Solution-Processed Tunable Spectral Response Photodetectors Enabled by Acidochromic Polymers

Advanced Electronic Materials

ADVANCED ELECTRONIC MATERIALS Open Access

www.advelectronicmat.de

RESEARCH ARTICLE OPEN ACCESS

Solution-Processed Tunable Spectral Response Photodetectors Enabled by Acidochromic Polymers

Pijush Kanti Aich[1] | Krzysztof Kotewicz[2] | Utkarsh Pandey[1] | Sobhan Hazra[1] | Ergang Wang[2] | Bhola Nath Pal[1]

[1]School of Materials Science and Technology, Indian Institute of Technology (Banaras Hindu University), Varanasi, India | [2]Department of Chemistry and Chemical Engineering, Chalmers University of Technology, Göteborg, Sweden

Correspondence: Ergang Wang (ergang@chalmers.se) | Bhola Nath Pal (bnpal.mst@iitbhu.ac.in)

Received: 12 February 2026 | **Revised:** 20 April 2026 | **Accepted:** 14 May 2026

Keywords: acidochromic polymers | detectivity | NIR detector | organic/inorganic heterojunction | oxide semiconductor | photodetector | responsivity | tunable band

ABSTRACT

Solution-processed tunable broadband photodetectors are fabricated by using acidochromic polymers in photodiode and phototransistor geometries with SnO_2/polymer p-n heterojunctions. This organic-inorganic heterojunction works as a rectifying junction and bilayer channel of the photodiodes and phototransistors, respectively. In both devices, the lower bandgap acidochromic polymers (PIDT-BAB, PIDT-BIB, and PIDT-BVB) work as the photoactive layer, whereas n-type SnO_2 works as the electron transport layer, and the devices show high spectrally selective blue and green sensitivity. The responsivity, detectivity, and response time of these photodiodes are in the range of 20–40 mA/W, 4–7.5 × 10^9 Jones, and ~7–10 s, respectively. The phototransistors are fabricated by using high-κ Li-Al_2O_3 gate dielectric, which enables them to reach their operating voltage within 2 V. Furthermore, the thin-film transistors (TFTs) show a large variation of threshold voltage with light intensity, with good linearity of variation with illumination power. The responsivity, detectivity, and response time of these phototransistors are in the same range as those of the photodiodes. Additionally, the spectral response of the photodiodes is tuned from the visible to the NIR region by using vapor-phase trifluoroacetic acid (TFA) due to their acidochromic effect in a reversible way, indicating their possible application as an optoelectrical switch.

1 | Introduction

Photodetectors are required to detect optical signal in different areas of electronics and optoelectronics [1, 2]. Among the different classes of photodetectors, visible light sensitive photodetectors have been widely used in various fields, such as environmental sensing, medical diagnostics, and optical communications [3, 4]. In the optical communication like light fidelity (Lifi) technology, near infra-red (NIR) lights commonly used due to the wide range of frequency spectrum which is 10^4 higher than current radio frequency based communication system [5, 6]. In such an optical communication system, NIR photodetectors are essential components. Besides, NIR photodetectors are widely used in wireless communication, remote sensing, night vision cameras, etc. [7, 8]. Until now, a variety of materials have been used for the fabrication of photodetectors including 2D materials, metal-oxide semiconductors, organic/polymer materials, colloidal nanoparticles, carbon-based nanostructures, etc. Among them, metal-oxide-based photodetectors are attractive nowadays for their tenability, cost-effectiveness, and environmental

Pijush Kanti Aich and Krzysztof Kotewicz contributed equally to this work.

stability, enabling diverse applications across science, technology, and industry [9, 10]. Oxide semiconductors are being considered as potential active channel materials for transparent electronics due to their wide bandgaps [11]. Typical metal oxide like tin oxide (SnO_2) has a bandgap of 3.3 eV, which is wide enough to be transparent in the visible-light range. [12] Therefore, it is difficult to fabricate a high-performance visible/NIR photodetector using oxide semiconductors only. To resolve this issue, several efforts have been made to fabricate polymer/metal-oxide bilayer hybrid photodetectors where lower bandgap polymers generate photocurrent mostly whereas metal-oxide semiconductors serves as electron transport layer [13, 14]. In such organic–inorganic p-n heterojunction device, spectral band of the photodetectors is broadened due to the polymer component whereas overall performance of the devices are improved largely due to the significantly higher carrier mobilities of oxide semiconductors. Particularly for a phototransistor fabrication, metal oxides are used as the conducting channel of the transistor due to their high electron mobility, whereas lower bandgap organic/polymer layer is used as the photo-active layer of the device that effectively broadens the spectral sensitivity of the device [15].

Again, fabricating tunable-spectrum photodetectors is of high interest for various applications, particularly for NIR/IR sensitive photodetector development [16–18]. Acidochromic polymers are a class of materials that can be doped in the presence of particular acids, effectively reducing their optical bandgap and broadening the optical sensitivity of a photodetector. The capability of the bandgap modulation of these materials in the presence of acid can be utilized as a spectrally tunable photodetector or optical window. However, due to the heavy doping of these polymers, their conductivity is largely enhanced, and their semiconducting nature is lost, making them difficult to use in electronic devices, therefore rarely reported in literature [19]. This gap is herein addressed by using acidochromic polymers, PIDT-BAB, PIDT-BIB, and PIDT-BVB, with previously reported doping mechanism in the presence of trifluoroacetic acid (TFA) [20]. To our knowledge, no similar investigation was carried out at the time of writing, that would elucidate how acidochromic properties of conjugated polymers translate to the performance of photodetectors.

In this work, SnO_2/polymer semiconductor heterojunctions [21] were used to fabricate photodetectors (photodiode and phototransistor) through solution processing techniques [22]. The photodiode devices were fabricated on an ITO-coated glass substrate, serving as the bottom electrode with 12 nm layer of gold (Au) used as a semi-transparent top electrode. The lower bandgap acidochromic polymers of these devices served as a photoactive layer, whereas n-type SnO_2 acted as an electron transport layer. All the photodetectors showed high spectrally selective blue and green sensitivity that follows their absorption spectrum [23, 24]. A thin layer of Li-Al_2O_3 was used as gate dielectric of the phototransistors that enables to reach their operating voltage within 2 V [25, 26]. Besides, these phototransistors showed a large variation of threshold voltage with light intensity maintaining good linearity with illumination power. Moreover, the spectral response of the photodiode was tuned from visible to NIR region by using the vapor-phase TFA due to its acidochromic properties, indicating its possible application as an acid-induced optical switch.

2 | Results and Discussion

2.1 | Thin Film Characterization

XRD analysis (Figure S1) confirmed the polycrystalline nature of SnO_2 and the amorphous structure of Li-Al_2O_3 and Al_2O_3 films. The dielectric layers exhibited high optical transparency with bandgaps >5 eV (Figure S2), while the SnO_2/polymer bilayer showed absorption extending up to ~600 nm (Figure S3). AFM images revealed smooth surfaces with ~1 nm roughness, and cross-sectional analysis indicated layer thicknesses of ~90, 18, and 40 nm for the dielectric, SnO_2, and polymer, respectively (Figure S4). The dielectric films also demonstrated high capacitance (~250 nF/cm^2), low leakage current (0.1 μA/cm^2 at 2 V), and high breakdown voltage, confirming their reliability for device fabrication (Figure S6). Detailed data are provided in Section S1.

2.2 | Electrical Characterization of the Photodiodes

The photodiodes were fabricated on patterned ITO substrates with n-SnO_2/p-polymer heterostructure, shown in Figure 1a–c.

Three different polymers, PIDT-BAB, PIDT-BIB, and PIDT-BVB, were used for the photodiode (PD) fabrication with device geometries of (ITO/SnO_2/BAB/Au), (ITO/SnO_2/BIB/Au), and (ITO/SnO_2/BVB/Au), named as PD-1, PD-2, and PD-3, respectively. The molecular structures of the polymers are shown in Figure 2. All three polymer-based diodes showed decent rectifying behavior under ±1 V applied bias and the I-V characteristics under dark and light were recorded as shown in Figure 3. The optoelectronic properties of the photodiodes were investigated under different intensities of blue (peak intensity at 445 nm) and green (peak intensity at 520 nm) light illumination in ambient conditions, indicating that PDs have high photosensitivity under reversed bias with these respective lights. Figure 3a–c shows the I-V characteristics under the same intensities of the blue light for PD-1, PD-2, and PD-3, respectively, while Figure 3d–f corresponds to the green light illumination [27]. From these characteristics, it can be noted that the photocurrents have been enhanced by the factors of 22, 43, and 18 under blue light of 1.2 W/m^2 illumination in PD- 1, PD-2, and PD-3, respectively. However, the photocurrents have enhanced 28, 36, and 5 times under green light of the same intensity in PD-1, PD-2, and PD-3. In PDs, under optical illumination of blue and green lights, excitons are generated in the polymer layer mostly due to their lower bandgap, then separated into photoelectrons and photo holes due to the barrier potential of the p-n heterostructure [28]. Particularly, photoelectrons are transferred from the organic polymer to SnO_2, then to ITO, while holes are transferred from the polymer to the top gold (Au) electrode. Again, this photocurrent generation is more pronounced in reverse bias due to the faster collection of the photo-generated carriers.

2.3 | Electrical Characterization of the Phototransistors

The output (I_D-V_D) and transfer (I_D-V_G) characteristics of the SnO_2-only transistor (TFT-1, Figure S7a) are shown in

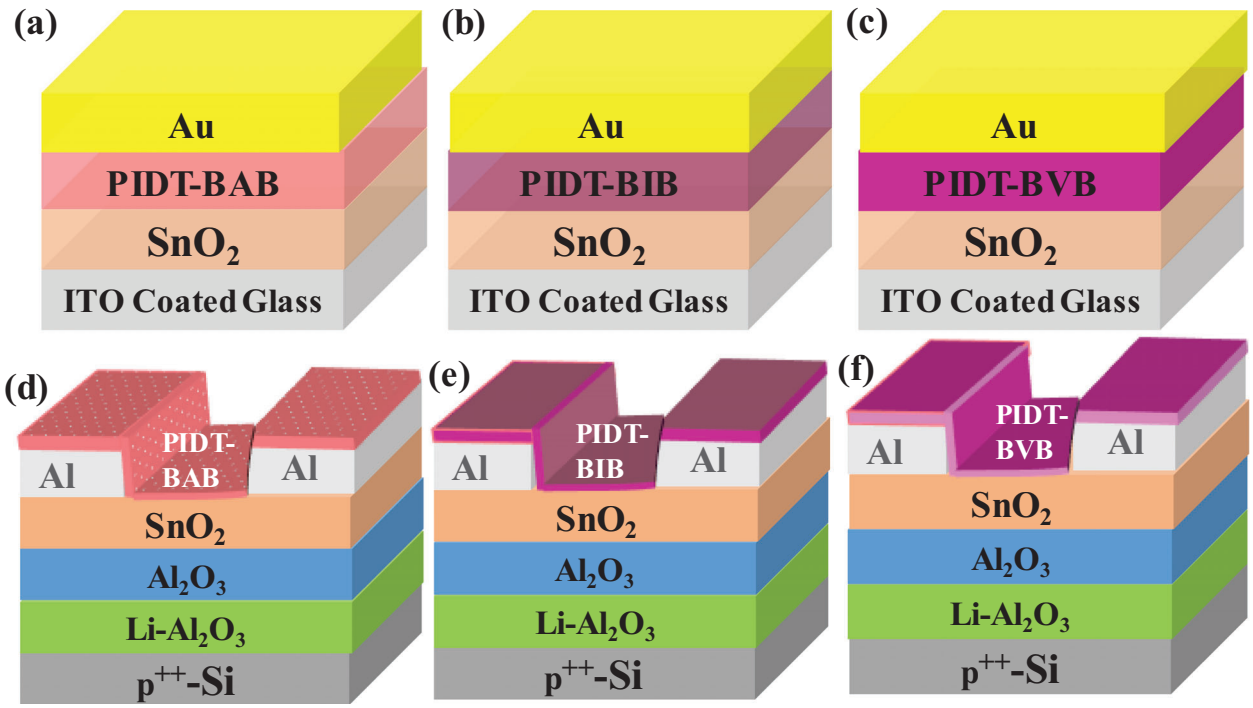

FIGURE 1 | Schematic diagram of two-terminal photodiodes with (a) SnO_2/PIDT-BAB heterojunction (PD-1), (b) SnO_2/PIDT-BIB heterojunction (PD-2), and (c) SnO_2/PIDT-BVB heterojunction (PD-3). The phototransistor with heterojunction channel of (d) SnO_2/PIDT-BAB (TFT-2), (e) SnO_2/PIDT-BIB (TFT-3), (f) SnO_2/PIDT-BVB (TFT-4).

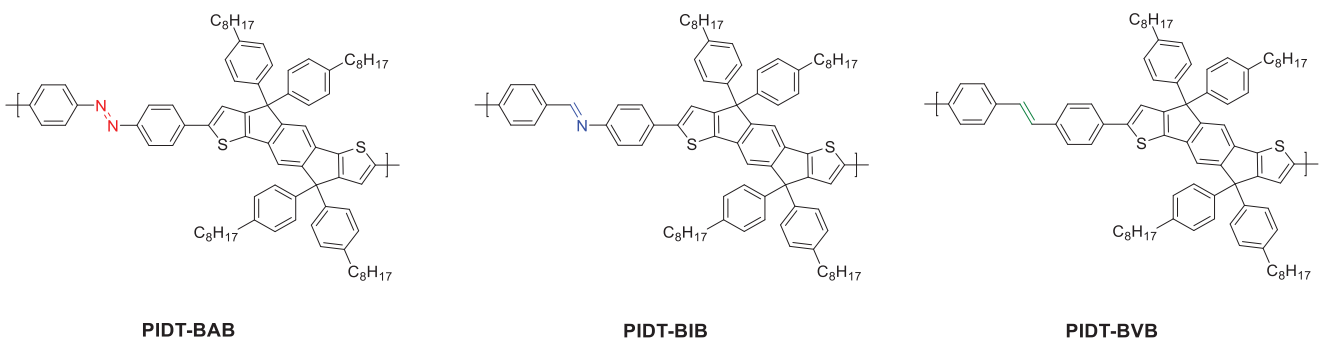

FIGURE 2 | The molecular structures of PIDT-BAB (left), PIDT-BIB (middle), and PIDT-BVB (right).

Figure S7b,c, respectively, indicating an n-channel transport of the device. Figure S7c shows that the threshold voltage (V_{th}) of this SnO_2 TFT is ~ −0.1 V with an On/Off ratio of 1.25×10^4, which is reasonably good for a 2 V operating voltage device. The transistor parameters like effective carrier mobility (μ) in the saturation region, subthreshold swing (SS), and the maximum density of the trap states ($N_{ss}{}^{max}$) can be calculated from the following equations:

$$\mu_{sat} = \frac{\left(\frac{\partial\sqrt{I_D}}{\partial V_G}\right)^2}{\frac{1}{2}\times\frac{W}{L}\times C} \quad (1)$$

$$SS = \left(\frac{\partial(\log I_D)}{\partial V_G}\right)^{-1} \quad (2)$$

$$N_{SS}^{max} = \left(\frac{SS\times \log e}{\left(\frac{kT}{q}\right)} - 1\right)\frac{C}{q} \quad (3)$$

where I_D, V_G, C, k, T, and q denote the saturation current, threshold voltage, areal capacitance, Boltzmann constant, temperature at the Kelvin scale, and electronic charge, respectively. The extracted saturation mobility of the SnO_2 TFT is 0.2 $cm^2\ V^{-1}\ s^{-1}$, whereas the SS value is 278 mV/dec. Besides, the device was illuminated with blue and green light with different intensities from 0 to 1.2 W/m^2, resulting in no significant difference in transfer characteristics, indicating this reference SnO_2 transistor doesn't show any blue and green light sensitivity (Figure S7d,e). Similarly, TFT-1 was also tested under different UV light illumination, showing a significant variation of drain current (Figure S7f). The optical behavior of this reference SnO_2 transistor implies that the

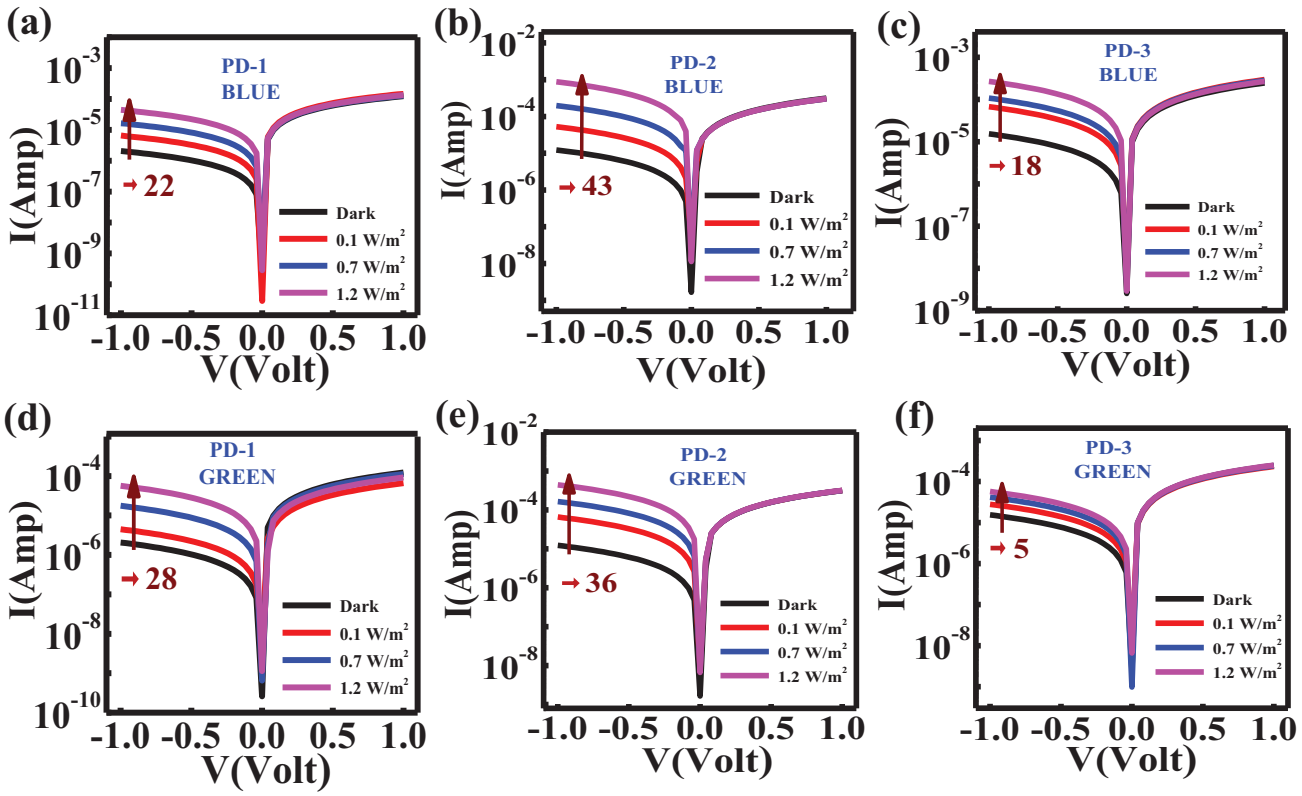

FIGURE 3 | I-V characteristics under light illumination of blue of (a) PD-1, (b) PD-2, and (c) PD-3. I-V characteristics under light illumination of green of (d) PD-1, (e) PD-2, and (f) PD-3.

TABLE 1 | Summary of device parameters of TFT-2, TFT-3, and TFT-4 under dark.

Device	Threshold Voltage (V_{th}) (volt)	Carrier Mobility ($cm^2\ V^{-1}\ s^{-1}$)	On-Off ratio	Subthreshold Swing ($mV.\ decade^{-1}$)	Interface Trap State Density (cm^{-2})
TFT-2	0.2	0.50	5.4×10^3	410	1.02×10^{13}
TFT-3	1.15	1.30	1.86×10^5	392	1.01×10^{13}
TFT-4	1.5	0.54	4.09×10^4	444	1.04×10^{13}

device has photosensitivity only for high-energy photons (such as UV light).

Analogously, TFT-2, TFT-3 and TFT-4 depicted in Figure 1d–f, underwent similar electrical characterizations. As TFT-1, these heterostructure devices exhibited clear current saturation in their output characteristics at an operating voltage of 2.0 V (Figure S8a,c,e). Besides, the on currents of the devices decrease with respect to the reference device (TFT-1). As a consequence, the effective carrier mobilities also change to 0.5, 1.3, and 0.54 $cm^2\ V^{-1}\ s^{-1}$ for TFT-2, TFT-3 and TFT-4, respectively. The transfer characteristics shown in Figure S8b,d,f, of the heterostructure devices gives the V_{th} value shifted toward positive voltage, which are 0.2, 1.15, and 1.5 V for TFT-2, TFT-3, and TFT-4, respectively. The On/Off ratio and subthreshold swing (under dark) of the TFTs remain almost identical. The device parameters of TFT-2, TFT-3, and TFT-4 in the dark condition are summarized in Table 1.

The optoelectrical response of the phototransistor was recorded under blue and green LEDs in ambient atmospheric conditions, similar to photodiodes. In contrast to photodiode devices, the drain current of phototransistors increases in both accumulation and depletion modes, although depletion mode enhancement is more pronounced. The UV photoresponse in the TFT-1 is quite high because of the UV sensitivity of the SnO_2 thin film. However, the electrical characterizations do not show any practical change under blue and green light. However, the optical response with the transfer characteristics (I_D-V_G) variation of TFT-2, TFT-3, and TFT-4 under blue (445 nm) light illumination is shown in Figure 4a–c respectively, while Figure 4d–f corresponds to green (520 nm) light illumination. As can be seen in Figure 4, TFT-2, TFT-3, and TFT-4 are responding both under blue as well as green light illumination of varying intensity 0.1 to 1.2 W/m^2. However, the photoresponses of these devices are more pronounced in the accumulation mode as compared to the depletion mode of the operation [29]. That is due to a larger variation in the accumulation mode current (On current) than the depletion

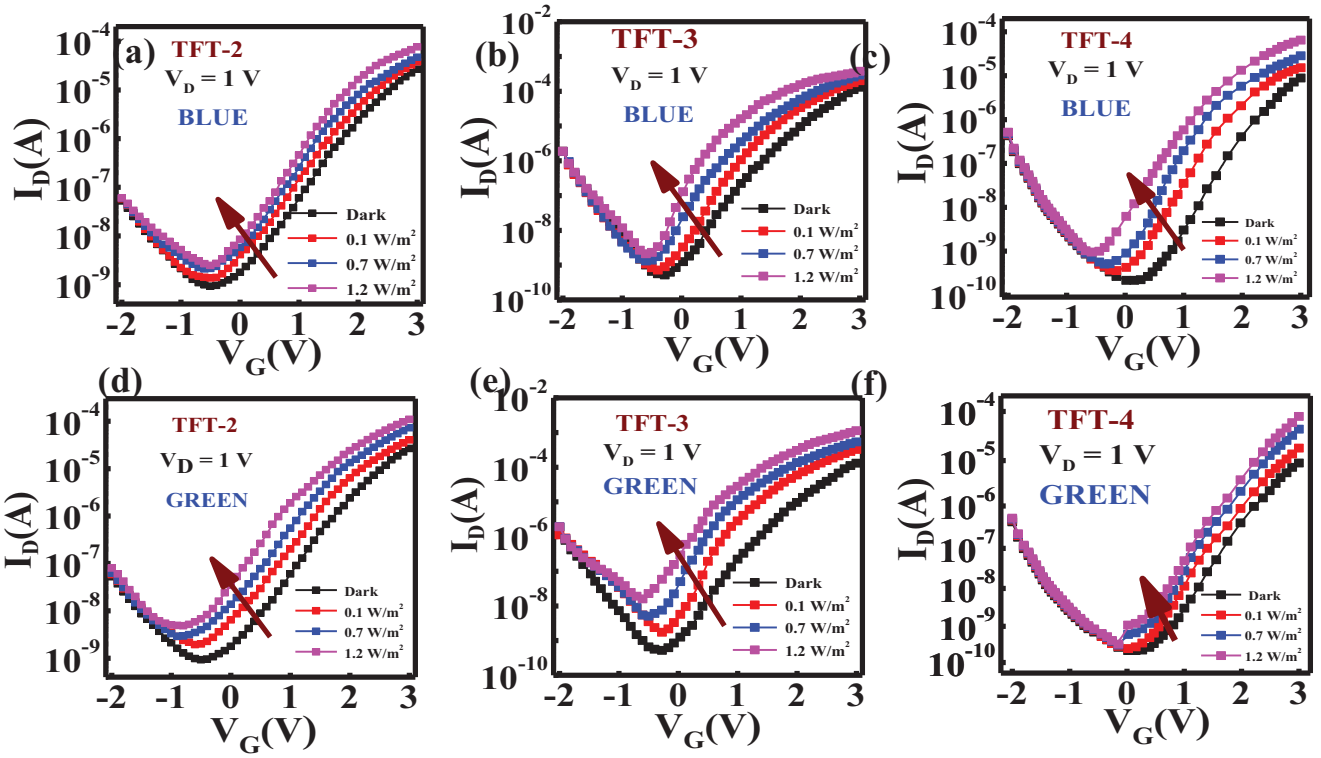

FIGURE 4 | Optical response phototransistor through transfer characteristics under blue of (a) TFT-2, (b) TFT-3, and (c) TFT-4. Optical response phototransistor under green of (d) TFT-2, (e) TFT-3, and (f) TFT-4.

mode current (Off current) [30]. Additionally, the threshold voltages of the TFTs decrease, resulting in a significant increase in photocurrent when illuminated by blue and green light [31, 32]. This accumulation current variation in the devices can be seen in the variation of drain current in the output characteristics devices, as shown in Figure S9. Overall, this study indicates that TFT-2 is more sensitive to the green light, whereas TFT-3 and TFT-4 have higher sensitivity to the blue light.

The variations in V_{th} of these phototransistors under illumination of different intensities were plotted as shown in Figure S10. These data show quite a linear variation of V_{th} with the intensity of light for all these organic/inorganic bilayer TFTs (S10 (a), S10 (b), and S10 (c)). Similarly, the on currents of the phototransistors have been increased at the cost of the V_{th} shifting in the devices, as well as additional carriers. The variations in the maximum on current (I_{max}) under blue and green light illuminations for these three devices are shown in Figure S10d–f, and are also quite linear.

2.4 | Transient Response of the Photodetectors

The device's response time, which dictates how quickly the detector can measure the subsequent signal, is another crucial characteristic of a photodetector [33]. The transient response of such devices is further investigated by illuminating them with blue and green light pulses with 445 and 520 nm of 1.2 W/m^2 intensity, while the photodiode is subjected to a 1 V external bias. The transient photoresponse of PD-1 under green light illumination has been shown in Figure 5a for multiple cycles, whereas Figure 5b shows a single-cycle response. Besides, the transient photoresponse of PD-2 and PD-3 is shown in Figure S11. From these data the rise times (τ_r) and decay times (τ_d) of the devices are calculated by defining the time intervals required for the 90% variation of the photocurrent from its initial value. The observed seconds-scale dynamics are consistent with extraction-limited transport in the SnO_2/polymer heterojunction, where the polymer side constitutes the bottleneck for hole collection. In such junctions, low effective hole mobility and trap-limited transport can lead to long carrier transit/collection times and a slow approach to steady photocurrent. Slow trap filling/emptying may also contribute; however, the persistence of second-scale dynamics after extended vacuum drying/annealing of the SnO_2/polymer heterojunction (to remove residual solvent) indicates that the response is not dominated by residual-solvent artifacts. Besides, the channel length of this OTFT is very large (~200 μm), which is ~ 10^3 times higher than a photodiode, and photogenerated carriers take a longer time to cross this distance, which is another reason for the slow photo-response of this device. The calculated rise times of PD-1, PD-2, and PD-3 are approximately 5.1, 2.9, and 3.6 s, while the corresponding decay times are approximately 1.9, 2, and 1.6 s, respectively.

The zero gate bias transient photoresponse investigation of the TFTs was carried out at 2 V drain bias under blue and green illumination with peak wavelengths, with the light power densities of 1.2 W/m^2. The transient photo-response of TFT-2 under green light illumination is shown in Figure 5c,d for multiple and single cycles, respectively. Under such conditions, the rise (τ_r) and decay time (τ_d) for TFT-2 are 9.8 and 12.2 s, respectively. TFT-3 and TFT-4 exhibit similar behavior, with rise

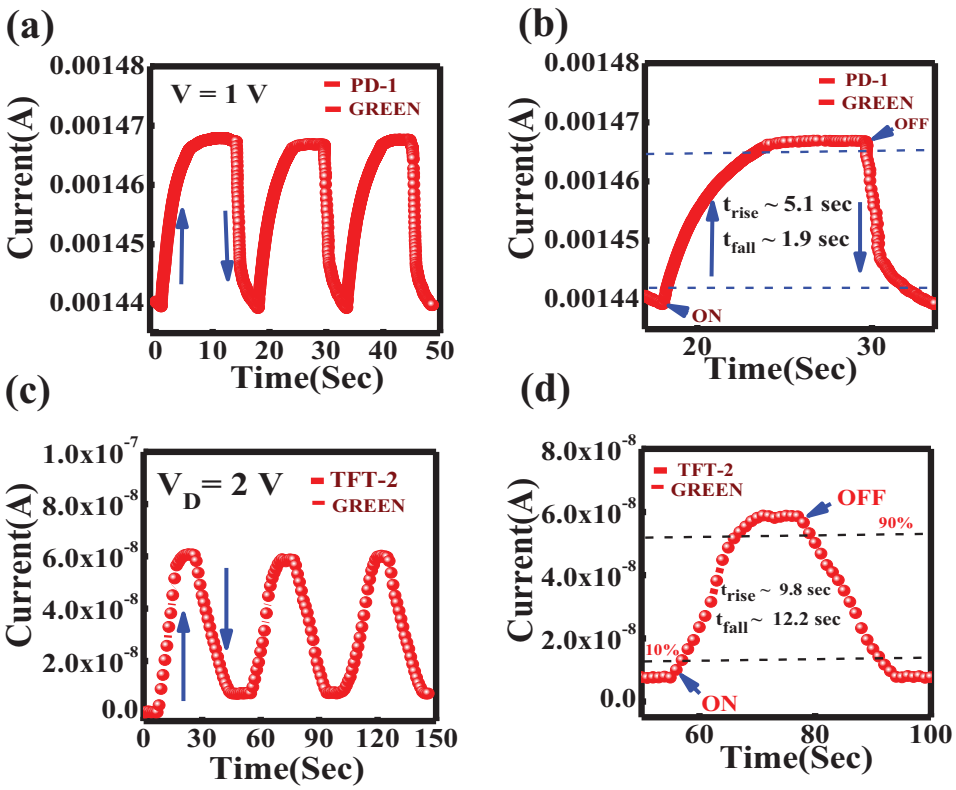

FIGURE 5 | Transient response of PD-1 under green light illumination in (a) multiple cycles and (b) single cycle; Transient response of TFT-2 under green light illumination in (c) multiple cycles and (d) single cycle.

times (τ_r) of 4.1 and 4.0 s, and decay times (τ_d) of 11.0 and 7.7 s, respectively, as shown in Figure S12.

2.5 | Photocurrent Spectra, Responsivity, and Detectivity of the Photodetector

One important metric that assesses a photodetector's capacity to transform incident photons into an electrical response is its external quantum efficiency (EQE). The EQE of a photodetector under illumination of a certain wavelength (λ) can be measured directly and related to responsivity (R_λ) by the following equation:

$$EQE = \frac{hcR_\lambda}{e\lambda} \quad (5)$$

where h, c, and e are the Planck constant, velocity of light, and charge of an electron, respectively. The EQEs of the devices were measured within the wavelength range from 300 to 700 nm, which describes the incident photon to photocurrent generation efficiency, are shown in Figure 6a–c for PD-1, PD-2, and PD-3, respectively. This measurement was performed under constant external bias of −1, −3, and −5 V. The EQE spectra of these devices showed good agreement for the device's optical absorption, in which the UV-range absorption originated from the SnO_2 layer, whereas absorption between 400–600 nm is due to the organic polymers. The UV region EQE of the photodiodes are 14%, 22.5%, and 13% at −5 V bias for PD-1, PD-2, and PD-3, respectively. It can also be noted that the second peaks are matched with the UV−Vis absorption spectra of PIDT-BAB, PIDT-BIB, and PIDT-BVB, as shown in Figure S3. This data also indicates that all three materials are blue and green-sensitive. The peak EQE values in the spectral range of 400–600 nm for PD-1, PD-2, and PD-3 are 5.5%, 9.6%, and 6.1%, respectively, which are measured at 450 nm under −5 V external bias. It can be noted that the EQE value of PD-2 is relatively higher w.r.t two other PDs, which is primarily due to different functional groups, which significantly influence their electronic interactions with the underlying semiconductor layer. These functional groups can alter the local charge distribution, interfacial dipoles, and energy-level alignment at the heterojunction interface, thereby modulating their charge transport behavior.

The Responsivity (R_λ) is an important parameter for evaluating the performance of a photodetector. EQE represents the photocurrent generated per incident photon, while R_λ quantifies the photocurrent produced per unit area of the photodetector when exposed to a unit power of light. Responsivity has been defined from the following equation:

$$R\lambda = \frac{I_{ph}}{\text{Power} \times S} \quad (4)$$

where $I_{ph} = I_{light}$-I_{dark}, S = light exposed area.

The change in the photo-responsivity of this photodiode under different external biases is depicted in Figure 6d–f. These data indicate that, under an external gate bias of −5 V, the peak

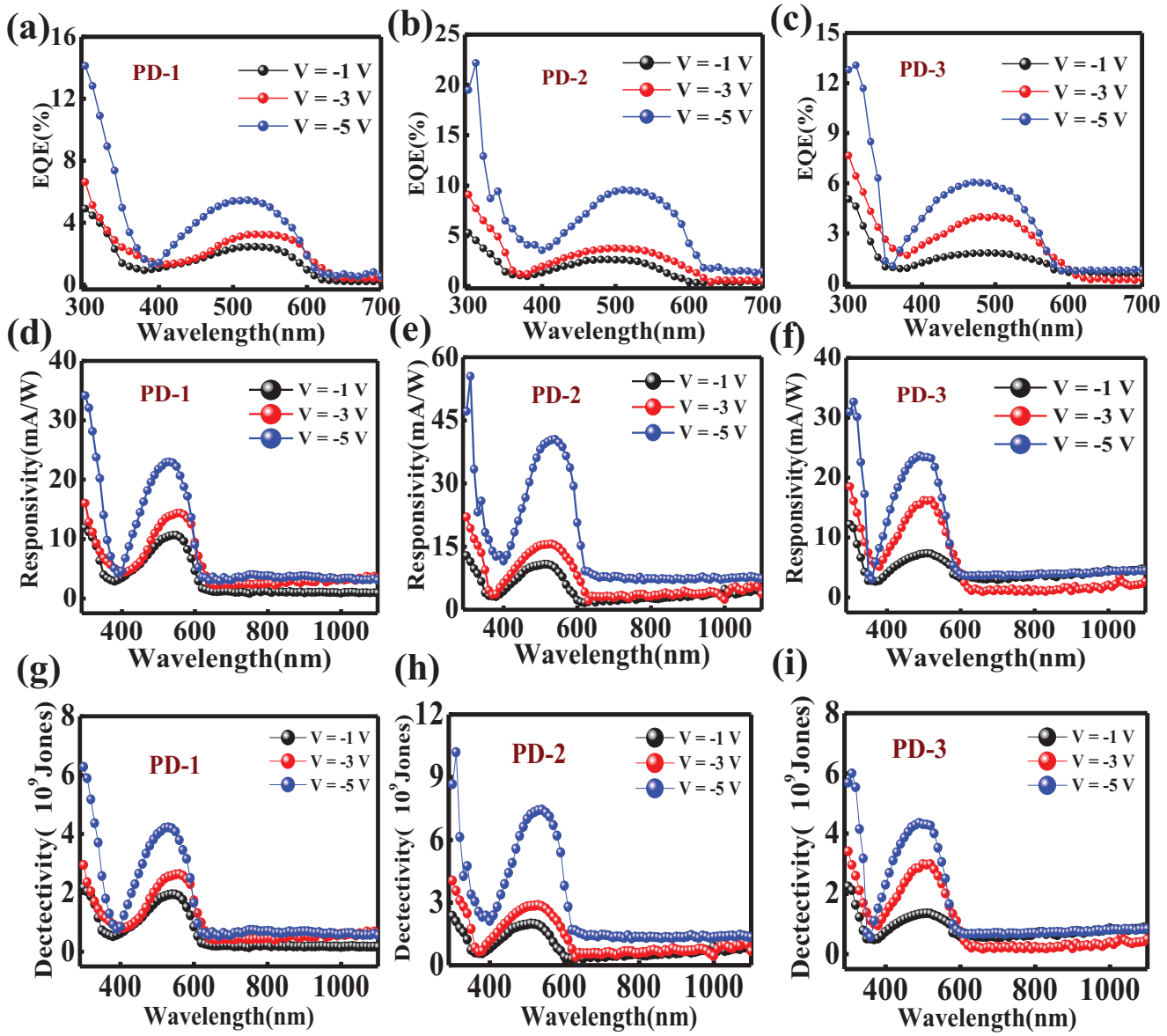

FIGURE 6 | External quantum efficiency vs wavelength spectra of (a) PD-1, (b) PD-2, and (c) PD-3; Responsivity vs wavelength spectra of the (d) PD-1, (e) PD-2, and (f) PD-3: Detectivity vs. wavelength spectra of (g) PD-1, (h) PD-2, and (i) PD-3.

responsivity (around 450 nm) of PD-1, PD-2, and PD-3 are 23, 41, and 24 mA/W, respectively.

Moreover, the specific detectivity D^* of a photodetector is a measure of its signal-to-noise ratio over a 1 Hz bandwidth, normalized to the detector's area [34]. This critical parameter characterizes the sensitivity of the detector. In this work, we considered shot noise is the primary source of noise, which originates from the device's dark current, not verified from experimental measurement, and based on this, D^* can be expressed as:

$$\mathrm{D}* = \frac{R_\lambda}{(2eJ)^{1/2}} \tag{6}$$

where J is the dark current density of the devices. The variation of the detectivity of the hetero-structure device is shown in Figure 6g–i, respectively for three devices under −1, −3, and −5 V external bias. The peak detectivity of this heterojunction photodiodes is observed with a value of 4.2×10^9 Jones for PD-1, 7.4×10^9 Jones for PD-2, and 4.5×10^9 Jones for PD-3, respectively under the external bias of −5 V. The summary of the peak values of the photodiode device parameters under −5 V external bias is shown in Table 2.

For the measurement of responsivity of phototransistors, devices were illuminated by the monochromatic light source of various wavelengths under the drain voltage (V_D) of 1 V with gate voltage of 2 and 3 V. The responsivity data, as depicted in Figure 7a–c show the peak responsivity of 1.92 A/W, 10.55 A/W and 1.83 A/W at 3 V gate voltage for TFT-2, TFT-3, and TFT-4, respectively. From the responsivity data, the EQE values were extracted, which are shown in Figure 7d–f. In the UV region (EQE due to SnO_2 semiconductor) the peak values of EQE are 2400%, 6000%, and 1600% for TFT-2, TFT-3, and TFT-4, respectively at 300 nm whereas in the visible region these values are 520%, 2950%, and 510% respectively for the three TFTs respectively. The high EQE

TABLE 2 | Summary of the peak values of photodiode device parameters under −5 V external bias in the visible region.

Device	EQE(%)	Responsivity(mA/W)	Detectivity(Jones)
PD-1	5.45	23	4.2×10^9
PD-2	9.56	40.5	7.4×10^9
PD-3	6.05	23.7	4.5×10^9

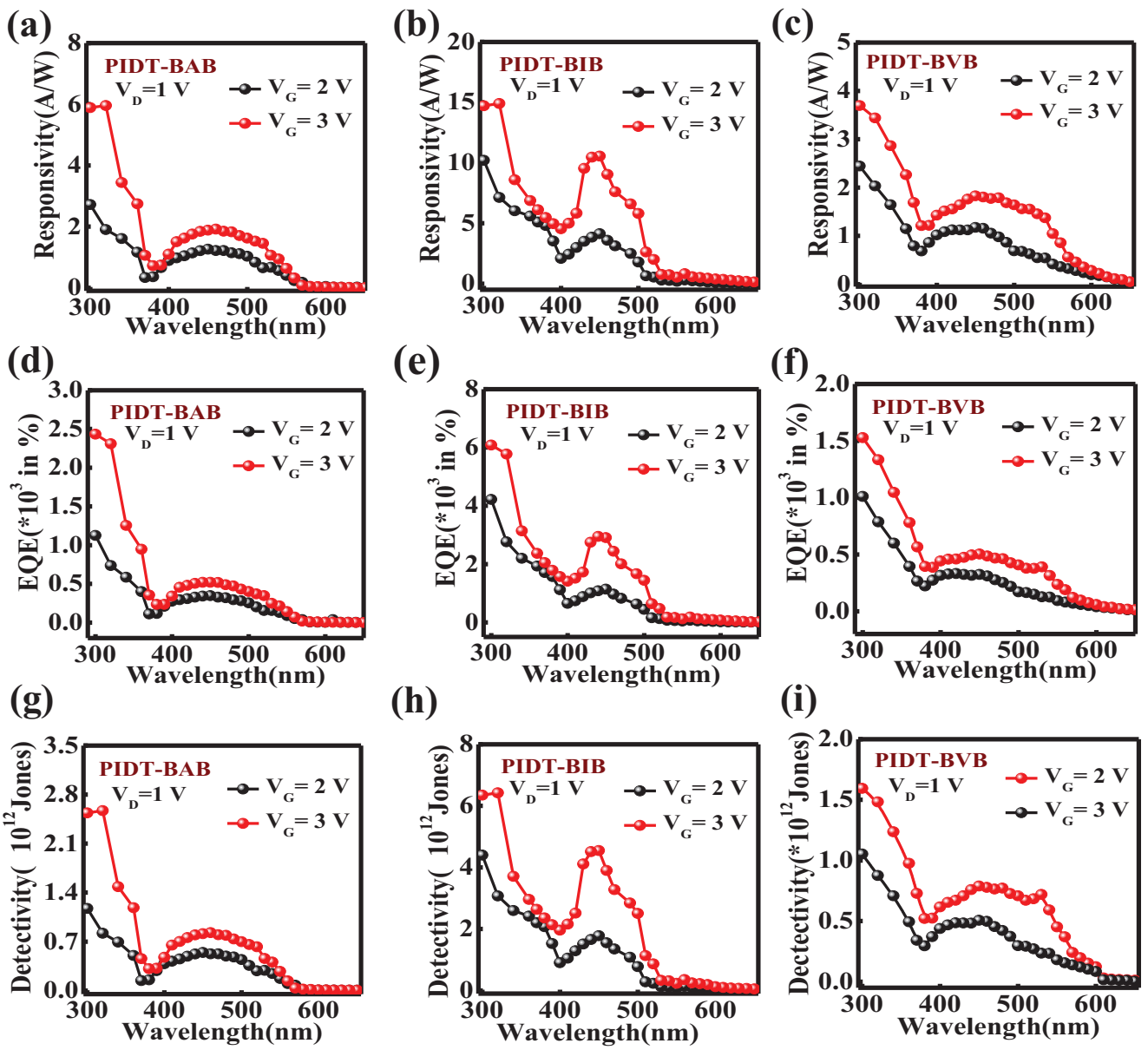

FIGURE 7 | Responsivity vs. wavelength spectra of the (a) TFT-2, (b) TFT-3 and (c) TFT-4; External quantum efficiency vs wavelength spectra of (d) TFT-2, (e) TFT-3 and (f) TFT-4; Detectivity vs. wavelength spectra of (g) TFT-2, (h) TFT-3 and (i) TFT-4.

values of the phototransistors are obtained due to photocurrent gain of phototransistor that are measured in accumulation mode. This gain is likely related to photogating or trap-assisted gain processes at the SnO_2/polymer interface. Photoexcited carriers generated in the polymer can become temporarily trapped, and allow multiple charge carriers to circulate per absorbed photon, thereby amplifying the photocurrent. Again, dark current of these phototransistors is also very high due to high channel current in accumulation mode (>10^{-6} A), which is the major source of noise. Therefore, instead of having very high EQE, the detectivity of these devices is limited. The extracted detectivity data of these TFTs are shown in Figure 7g–i have values of 5.4×10^{11}, 1.8×10^{12} and 5.1×10^{11} Jones for TFT-2, TFT-3, and TFT-4, respectively. The summary of the visible range peak values of the photo-transistors parameters under external V_G = 3 V and V_D = 1 V is given in Table 3.

TABLE 3 | Summary of the peak values of phototransistor device parameters under $V_G = 3$ V, $V_D = 1$ V in visible region.

Device	Responsivity(A/W)	EQE(%)	Detectivity(Jones)
TFT-2	1.92	520	5.4×10^{11}
TFT-3	10.55	2950	1.8×10^{12}
TFT-4	1.83	505	5.1×10^{11}

3 | Tuning the Spectral Range of Photosensitivity Through Acid Doping

In addition to the photosensitivity of these polymers to visible light, their potential to tune their spectral response from visible to near-infrared (NIR) in the presence of acid vapor due to their acidochromic nature was demonstrated. In a previous study, the mechanism of this behavior was investigated in detail. The structures of the three polymers differ in the nature of the double bond between the benzene rings of the repeat units. PIDT-BAB features an azo (N═N), PIDT-BIB an imine (C═N), and PIDT-BVB a vinyl (C═C) moiety. UV–vis absorption spectra of the polymer solutions in chloroform, before and after the addition of TFA, are shown in Figure S13. As can be seen from the figure, the presence of a free electron pair on a nitrogen atom strongly influences the molecule's response to an acidic environment. PIDT-BAB exhibited an exceptional bathochromic shift of 510 nm (corresponding to a 1.20 eV change in optical bandgap). Further spectroscopic characterization and DFT modeling revealed that the PIDT-BAB and PIDT-BIB undergo protonation at nitrogen atoms, while PIDT-BVB undergoes an acid doping process with polaron formation. The unusually strong absorption shift in PIDT-BAB was attributed to strong planarization of the polymer upon protonation and, therefore, an increase in the effective conjugation length [20]. The distinct acid–polymer interaction pathways directly translate into the different device-level spectral tuning behaviors. Because PIDT-BAB and PIDT-BIB undergo N-protonation accompanied by enhanced backbone planarization (and thus a larger effective conjugation increase), their photodiodes show pronounced red-shifts of the photoresponse upon TFA exposure, whereas PIDT-BVB primarily forms polarons without the same protonation-driven planarization and therefore does not exhibit a comparable EQE red-shift. Consistently, under identical TFA treatment, PD-1 shows the largest migration of the EQE toward the NIR, PD-2 shows a smaller red-shift, and PD-3 shows essentially no spectral shift, establishing a clear structure–doping–spectral response relationship across the polymer series. Overall, these results suggest a simple design rule for acidochromic spectral tuning: incorporating protonatable nitrogen bridges (azo/imine) enables strong, reversible red-shifts via protonation/planarization, whereas non-protonatable vinyl bridges favor polaronic doping with minimal EQE spectral migration.

To explore this phenomenon in photodetectors, the current-voltage (I-V) characteristics of the devices were recorded under ambient conditions in the presence of trifluoroacetic acid (TFA). During electrical characterization, a vapor of a TFA solution (molar ratio 1:10, TFA: DI water) was sprayed onto the device surface through a bottle jet sprayer. The I-V response of the device in contact with acid shows an enhancement of the depletion mode current, which is shown in Figure S14. Besides, PD-1 shows very good IR (950 nm) sensitivity (Figure S14a), whereas PD-2 shows red (640 nm) sensitivity (Figure S14b) and PD-3 shows blue (445 nm) sensitivity (Figure S14c), respectively.

Further, similar studies have been performed under low concentrations (~2% v/v) of strong acids like HCl, H_2SO_4, and HNO_3. A quantitative comparison of the acidochromic and photoresponses of PIDT-BAB under TFA (~8% v/v), HNO_3 (~2% v/v), HCl (~2% v/v), and H_2SO_4 (~2% v/v) vapors is shown in Figure S15. Figure S15a represented the I-t response before and after different acid treatment of PD-1, indicating approximately two orders of enhancement of current for PD-1 under dark conditions. The enhancement of the dark current of the PD is due to the heavy doping of acidochromic polymers. Figure S15b presents the photo-response under long (~250 s) NIR illumination (for PD-1) in the presence of these acid vapors. A clear enhancement of the current level is observed in all cases. Upon treatment with TFA, the current level of the device started decreasing after 40 s due to the evaporation of TFA, which de-doped the polymer. However, in the case of strong acids, this current sustains longer time due to their higher boiling point. Since H_2SO_4 has the highest boiling point among these acids, it took the longest time (>250 s) to decay.

To realize the spectral variation of photosensitivity in the presence of TFA vapor, EQE measurements were performed in all of these three photodetectors, which are shown in Figure 8a–c. Out of these devices, PD-1 shows a larger NIR shift of the spectrum (Figure 8a). Moreover, its photosensitivity in the visible range disappears. Besides, this device has significant external voltage-dependent photocurrent generation. At -5 V bias, PD-1 shows an EQE value of ~10% at 1010 nm. Although PD-2 shows relatively lower shifts in spectra, and PD-3 shows no spectral shift but has similar voltage-dependent EQE, which are shown in Figure 8b,c, respectively. These results are consistent with TFA-induced charge transfer/protonation, generating additional sub-gap absorption features and altering the dominant photogeneration pathway. Accordingly, the NIR photoresponse observed after TFA exposure is attributed to acid-induced electronic states (e.g., polaronic/protonated species) rather than a simple rigid shift of the original neutral π–π^* transition. A full assignment of these states would require complementary spectroscopic/electronic-structure analysis and is beyond the scope of this work.

The temporal evolution of the current response of photodiodes was systematically recorded as a function of time immediately after the application of the TFA spray. This measurement allowed for detailed monitoring of the dynamic changes in conductivity induced by acid under illumination, providing insights into the material's acidochromic switching behavior. During this study, light was illuminated in entire period of measurement

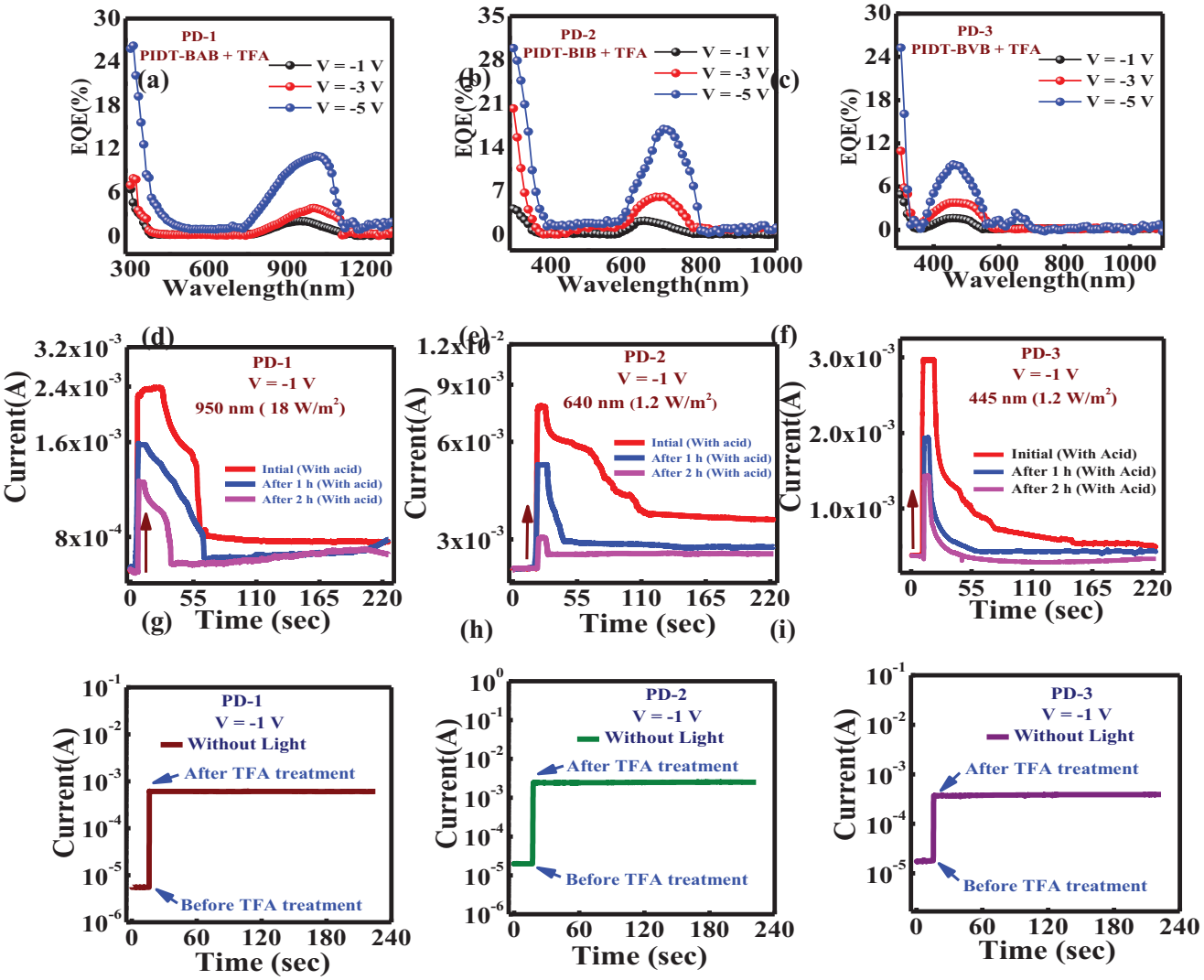

FIGURE 8 | External quantum efficiency vs. wavelength spectra after TFA treatment of (a) PD-1, (b) PD-2, and (c) PD-3; Transient photo response under different light after TFA treatment of (d) PD-1 (IR light), (e) PD-2 (Red light), (f) PD-3 (Blue light) with trifluoroacetic acid effect; Current Vs. time (I-t) data before and after TFA treatment under dark of (g) PD-1, (h) PD-2, (i) PD-3.

(~220 s). The transient response of PD-1 was measured at −1 V bias under IR (950 nm) light illumination with a power density of 18 W/m^2 (shown in Figure 8d). Since TFA possesses a low boiling point, it gradually evaporates over time, allowing the polymer to revert to its initial state. Consequently, the current response decays back to its original baseline level. The I-t response was recorded at 1 and 2 h after the initial measurements, revealing a reduced current level compared to the initial response. Figure 8e presents the I-t response of PD-2 under red light illumination (640 nm). Since PIDT-BVB exhibits no spectral changes upon acid treatment [20], Figure 8f displays the I-t response of PD-3 under blue light illumination (445 nm). Besides, I-t response before and after TFA treatment of PD-1, PD-2, and PD-3 are shown in Figure 8g–i, respectively, indicating ~ two orders of enhancement of current for PD-1 and PD-2, whereas this enhancement is > one order higher for PD-3 under dark conditions. Enhancement of dark current of the PDs originated due to the heavy doping of acidochromic polymers, due to the TFA treatment.

4 | Conclusions

In conclusion, solution-processed organic/inorganic p-n heterojunction photodetectors have been fabricated with tunable band photosensitivity by using acidochromic organic polymers like PIDT-BAB, PIDT-BIB, and PIDT-BVB. These polymers exhibit visible absorption in the neutral state and, upon exposure to acid vapor, develop acid-induced electronic states that extend the photoresponse toward the near-infrared, providing a route to spectral tuning without relying on intrinsically narrow-bandgap polymers. The hybrid devices were realized in both photodiode and phototransistor geometries and show strong visible-light photoresponse; detectivity values are reported as shot-noise-limited estimates (upper bounds) based on the dark current. Upon TFA exposure, the photodiode photoresponse red-shifts from the visible toward the NIR, and the effect is transient and at least partially reversible as the acid evaporates. Together, these results establish a proof-of-concept platform for acid-responsive tuning of photodetector spectral sensitivity and

motivate future work toward fully noise-validated metrics and multi-cycle stability.

5 | Experimental Section

5.1 | Material Synthesis

Lithium acetate and aluminium nitrate (non-hydrate) were used to prepare a precursor solution of Li-Al_2O_3 [35]. A concentration of 500 mM was taken for both solutions, which were prepared separately by dissolving in 2-methoxyethanol (2-MEA). After that, these two solutions were mixed in a volume ratio of 1:11 and vigorously stirred for 6 h and left for 48 h of aging before the thin film deposition. A 100 mM precursor solution of aluminium nitrate (non-hydrate) was also prepared for Al_2O_3 thin film deposition. Similarly, tin chloride (Sigma Aldrich) was dissolved in 2-MEA to prepare a 100 mM precursor solution for SnO_2 semiconductor thin film deposition [36]. Previously reported indacenodithiophene-based acidochromic conjugated polymers, PIDT-BAB, PIDT-BIB, and PIDT-BVB, were used as acidochromic polymer for this study [20]. The polymers were dissolved in toluene separately at a concentration of 3 mg/ml and sonicated for 5 min in chilled DI water.

5.2 | Device Fabrication

Prior to the fabrication of the photodiode, several patterned ITO-coated glass substrates (size of 15 × 15 mm) were subjected to a wet cleansing process. The substrates were cleaned using a soap solution and then sonicated for 15 min in each of the following solvents: DI water, acetone, and isopropanol. The substrates were exposed to oxygen plasma for 10 min in order to make the surface hydrophilic and remove any organic residues. Subsequently, the glass substrates were dried using a hot plate set at a temperature of 100°C for 5 min. This drying process effectively removed any remaining moisture from the substrate. After that, the cleaned substrates were spin-coated with SnO_2 semiconductor at 4000 rpm for 40 s, and dried at 90°C for 5 min. To obtain the desired thickness, this process was repeated once more, and the film was annealed 500°C for 30 min. After that, polymer materials (PIDT-BAB, PIDT-BIB, and PIDT-BVB) were spin-coated on different substrates at 1000 rpm for 40 s and subsequently dried at 80°C for 30 min by keeping them inside a vacuum oven to remove solvent from the film completely. A 12 nm semi-transparent gold (Au) film was deposited on top of the polymer layer that works as an electrode. The photodiodes made of PIDT-BAB, PIDT-BIB, and PIDT-BVB polymer are called PD-1, PD-2, and PD-3, respectively (shown in Figure 1a–c). A trifluoroacetic acid (TFA) solution in 10:1 (TFA: DI water) ratio was prepared to be sprayed on the devices.

Besides, bottom-gate top contact SnO_2/polymer heterostructure thin film transistors (TFT) were fabricated using a solution process method atop a highly p-doped silicon (p^{++}-Si) substrate in order to show the photosensitivity of these acidochromic polymers. A Li-Al_2O_3 thin film was used as gate dielectric of these TFTs, which reduces its operating voltage to 2 V. At the beginning, cleaned p^{++}-Si substrates were spin-coated with a 500 mM precursor solution of Li-Al_2O_3 dielectric at 5000 rpm for 50 s followed by an annealing process at 350°C for 30 min. To obtain the desired thickness, this process was repeated twice and finally annealed at 500°C for 1 h. To lessen the Li-Al_2O_3 dielectric's surface roughness, a thin layer of Al_2O_3 was deposited on top of it. During this deposition, the precursor solution of Al_2O_3 was spin-coated at 3000 rpm for 30 secs and annealed at 300°C for 45 min. A tin-oxide (SnO_2) solution was spin coated on top of gate dielectric at 4000 rpm for 40 s and annealed at 500°C for 30 min a to get polycrystalline film of SnO_2 [37]. To deposit the source-drain contact for the TFTs, aluminium(Al) with a thickness of 70 nm was thermally evaporated on top of the SnO_2 film using a shadow mask that forms a channel of the TFTs with a width-to-length ratio (W/L) of 118 (23.6 mm/0.2 mm). Following Al deposition, photosensitive materials were spin-coated on the substrates. This SnO_2 TFT has been studied as a reference device and called as TFT-1. Besides, acidochromic polymers were spin-coated on top of SnO_2 TFTs with a speed of 1000 rpm for 1 min. The TFTs coated with PIDT-BAB, PIDT-BIB, and PIDT-BVB are named as TFT-2, TFT-3 and TFT-4, respectively (shown in Figure 1d–f).

5.3 | Material and Device Characterization

A tabletop X-ray diffractometer (A Rigaku Mini Flex 600, DTEX) was used to examine the phase and crystallinity of various materials and films. An NTMDT-NTEGRA-prima atomic force microscope (AFM) was used to analyze the surface topographies of thin films. For cross-sectional scanning electron microscopy (SEM), Apreo 2 SEM (Thermo Fisher Scientific) was used. UV–Vis spectroscopic studies and EQE of photodiodes were performed using EnliTech QE-R. An LCR meter (Keysight Technology Model E4990A) was used to study the capacitance vs frequency (C-f) spectra of the dielectric films. A semiconductor parametric analyzer (Keysight B1500A) and a source meter (Keysight B2912A) were used to perform all electrical characterizations under ambient conditions. Gate voltage dependent EQE of phototransistors were studied through SQR300F spectra MONOCHROMATOR.

Author Contributions

B.N.P. and E.W. conceived the idea. K.K. synthesized the materials and carried out the characterization. P.K.A. and U.P. fabricated the devices and carried out the measurements. S.H. performed and supported the device characterization. P.K.A. and K.K. conducted the literature review. P.K.A. structured and wrote the original version of the manuscript, and all authors discussed the results and contributed to the final production of the manuscript.

Acknowledgment

Bhola Nath Pal thanks the DST (India) for financial support of the Indo-Sweden project (DST/INT/SWD/VR/P-12/2019) and partial support from SERB, India (CRG/2019/001826). The authors are also grateful to the Central Instrument Facility Centre, IIT (BHU), for providing instrument support for AFM. Pijush Kanti Aich acknowledges UGC for providing the SRF fellowship. Utkarsh Pandey acknowledges MoE-STARS (MoE-STARS/STARS-2/2023-0479) for granting financial support. Sobhan Hazra acknowledges IIT(BHU) for providing a SRF fellowship. Ergang Wang thanks the Swedish Research Council for the financial support of the Indo-Sweden project (Project No: 2018–07072).

Conflicts of Interest

The authors declare no conflicts of interest.

Data Availability Statement

The data that support the findings of this study are available from the corresponding author upon reasonable request.

References

1. Y. Xu and Q. Lin, "Photodetectors Based on Solution-Processable Semiconductors: Recent Advances and Perspectives," *Applied Physics Reviews* 7, no. 1 (2020): 011315, https://doi.org/10.1063/1.5144840.

2. K. Gundepudi, P. M. Neelamraju, S. Sangaraju, et al., "A Review on the Role of Nanotechnology in the Development of Near-Infrared Photodetectors: Materials, Performance Metrics, and Potential Applications," *Journal of Materials Science* 58, no. 35 (2023): 13889–13924, https://doi.org/10.1007/s10853-023-08876-8.

3. K.-H. Lee, D.-S. Leem, J. S. Castrucci, et al., "Green-Sensitive Organic Photodetectors with High Sensitivity and Spectral Selectivity Using Subphthalocyanine Derivatives," *ACS applied materials & interfaces* 5, no. 24 (2013): 13089–13095, https://doi.org/10.1021/am404122v.

4. J.-H. Lu, B.-H. Jiang, F.-C. Hsiao, et al., "High-Performance Organic Photodiodes for Blue-Light Hazard Detection," *Chemical Engineering Journal* 437 (2022): 135327, https://doi.org/10.1016/j.cej.2022.135327.

5. S. Khan, M. Usman, and S. Ali, "Perspective on Light-Fidelity and Visible Light Communication," *Journal of Laser Applications* 34, no. 1 (2022): 011202, https://doi.org/10.2351/7.0000614.

6. C. Chen, D. A. Basnayaka, A. A. Purwita, X. Wu, and H. Haas, "Wireless Infrared-Based LiFi Uplink Transmission with Link Blockage and Random Device Orientation," *IEEE Transactions on Communications* 69, no. 2 (2021): 1175–1188, https://doi.org/10.1109/TCOMM.2020.3035405.

7. Y. Zhu, C. Geng, L. Hu, et al., "Skin-Like Near-Infrared II Photodetector with High Performance for Optical Communication, Imaging, and Proximity Sensing," *Chemistry of Materials* 35, no. 5 (2023): 2114–2124, https://doi.org/10.1021/acs.chemmater.2c03701.

8. M. I. Saleem, A. K. K. Kyaw, and J. Hur, "Infrared Photodetectors: Recent Advances and Challenges toward Innovation for Image Sensing Applications," *Advanced Optical Materials* 12, no. 33 (2024): 2401625, https://doi.org/10.1002/adom.202401625.

9. M. S. Chavali and M. P. Nikolova, "Metal Oxide Nanoparticles and Their Applications in Nanotechnology," *SN Applied Sciences* 1, no. 6 (2019): 607, https://doi.org/10.1007/s42452-019-0592-3.

10. W. Ouyang, F. Teng, J. H. He, and X. Fang, "Enhancing the Photoelectric Performance of Photodetectors Based on Metal Oxide Semiconductors by Charge-Carrier Engineering," *Advanced Functional Materials* 29, no. 9 (2019): 1807672, https://doi.org/10.1002/adfm.201807672.

11. J. Y. Tsao, S. Chowdhury, M. A. Hollis, et al., "Ultrawide-Bandgap Semiconductors: Research Opportunities and Challenges," *Advanced Electronic Materials* 4, no. 1 (2018): 1600501, https://doi.org/10.1002/aelm.201600501.

12. J. Shi, J. Zhang, L. Yang, M. Qu, D. C. Qi, and K. H. Zhang, "Wide Bandgap Oxide Semiconductors: from Materials Physics to Optoelectronic Devices," *Advanced Materials* 33, no. 50 (2021): 2006230, https://doi.org/10.1002/adma.202006230.

13. A. Ullah, R. Lamug, X. Zhang, O. Ostroverkhova, and L.-J. Cheng, "Highly Sensitive and Fast-Response Hybrid Phototransistors Enabled by Dynamic Photogating in Anthradithiophene-Metal Oxide Heterojunctions," *Advanced Optical Materials* 13, no. 16 (2025): 2500081, https://doi.org/10.1002/adom.202500081.

14. Y. S. Rim, Y. M. Yang, S.-H. Bae, et al., "Ultrahigh and Broad Spectral Photodetectivity of an Organic–Inorganic Hybrid Phototransistor for Flexible Electronics," *Advanced Materials* 27, no. 43 (2015): 6885–6891, https://doi.org/10.1002/adma.201502996.

15. S. Nam, J. Seo, S. Park, et al., "Hybrid Phototransistors Based on Bulk Heterojunction Films of Poly (3-hexylthiophene) and Zinc Oxide Nanoparticle," *ACS applied materials & interfaces* 5, no. 4 (2013): 1385–1392, https://doi.org/10.1021/am302765a.

16. O. D. I. Moseley, B. Roose, S. J. Zelewski, S. Kahmann, K. Dey, and S. D. Stranks, "Tunable Multiband Halide Perovskite Tandem Photodetectors with Switchable Response," *ACS Photonics* 9, no. 12 (2022): 3958–3966, https://doi.org/10.1021/acsphotonics.2c01328.

17. P. Pertsch, R. Kullock, V. Gabriel, L. Zurak, M. Emmerling, and B. Hecht, "Tunable Nanoplasmonic Photodetectors," *Nano Letters* 22, no. 17 (2022): 6982–6987, https://doi.org/10.1021/acs.nanolett.2c01772.

18. J. Wang, S. Ullbrich, J.-L. Hou, et al., "Organic Cavity Photodetectors Based on Nanometer-Thick Active Layers for Tunable Monochromatic Spectral Response," *ACS Photonics* 6, no. 6 (2019): 1393–1399, https://doi.org/10.1021/acsphotonics.9b00471.

19. Y. Wang, Q. Chen, Z. Liu, et al., "Acidochromic Organic Photovoltaic Integrated Device," *Chemical Engineering Journal* 452 (2023): 139479, https://doi.org/10.1016/j.cej.2022.139479.

20. K. Kotewicz, L. R. Franco, M. Araujo, and E. Wang, "Acidochromic Behaviors of Indacenodithiophene-Based Conjugated Polymers Containing Azo, Imine, and Vinyl Bonds," *Macromolecules* 58, no. 5 (2025): 2719–2729, https://doi.org/10.1021/acs.macromol.4c02700.

21. S. Dahiya, S. V. Singh, U. Pandey, S. Hazra, and B. N. Pal, "Microwave-Assisted Synthesis of CuZnS Nanocrystals for Spectrally Flat Visible Light Photodetector Application Using a ZnO/CuZnS Heterojunction," *ACS Applied Optical Materials* 2, no. 5 (2024): 776–783.

22. B. N. Pal, B. M. Dhar, K. C. See, and H. E. Katz, "Solution-Deposited Sodium Beta-Alumina Gate Dielectrics for Low-Voltage and Transparent Field-Effect Transistors," *Nature materials* 8, no. 11 (2009): 898–903, https://doi.org/10.1038/nmat2560.

23. S. Suman, S. Dahiya, R. P. Jaiswal, P. Swaminathan, and B. N. Pal, "Fabrication of a Red-Sensitive Heterojunction Photodetector by Using a Narrowband Organic Dye," *The Journal of Physical Chemistry C* 127, no. 38 (2023): 19182–19188, https://doi.org/10.1021/acs.jpcc.3c04112.

24. A. Sharma, N. K. Chourasia, A. Sugathan, et al., "Solution Processed Li_5AlO_4 Dielectric for Low Voltage Transistor Fabrication and Its Application in Metal Oxide/Quantum Dot Heterojunction Phototransistors," *Journal of Materials Chemistry C* 6, no. 4 (2018): 790–798, https://doi.org/10.1039/C7TC05074G.

25. N. Pal, A. Sharma, V. Acharya, N. K. Chourasia, S. Biring, and B. N. Pal, "Gate Interface Engineering for Subvolt Metal Oxide Transistor Fabrication by Using Ion-Conducting Dielectric with Mn_2O_3 Gate Interface," *ACS Applied Electronic Materials* 2, no. 1 (2019): 25–34, https://doi.org/10.1021/acsaelm.9b00641.

26. U. Pandey, N. K. Chourasia, N. Pal, S. Biring, and B. N. Pal, "Functional Dielectric Properties of Solution-Processed Lithium Indium Tin Oxide ($LiInSnO_4$) and Its Application as a Gate Insulator of a Low Voltage Thin Film Transistor," *IEEE Transactions on Electron Devices* 69, no. 3 (2022): 1077–1082, https://doi.org/10.1109/TED.2022.3147153.

27. O. Game, U. Singh, T. Kumari, A. Banpurkar, and S. Ogale, "ZnO (N)–Spiro-MeOTAD Hybrid Photodiode: an Efficient Self-Powered Fast-Response UV (visible) Photosensor," *Nanoscale* 6, no. 1 (2014): 503–513.

28. R. D. Jansen-van Vuuren, A. Armin, A. K. Pandey, P. L. Burn, and P. Meredith, "Organic Photodiodes: the Future of Full Color Detection and Image Sensing," *Advanced Materials* 28, no. 24 (2016): 4766–4802, https://doi.org/10.1002/adma.201505405.

29. K.-C. Lee, Y.-H. Chuang, and C.-K. Huang, "Photoresponse of Graphene Channel in Graphene-Oxide–Silicon Photodetectors," *Photonics* 10, no. 5 (2023): 568.

30. Y. Liu, X. Duan, H.-J. Shin, S. Park, Y. Huang, and X. Duan, "Promises and Prospects of Two-Dimensional Transistors," *Nature* 591, no. 7848 (2021): 43–53, https://doi.org/10.1038/s41586-021-03339-z.

31. M. G. Yun, Y. K. Kim, C. H. Ahn, et al., "Low Voltage-Driven Oxide Phototransistors with Fast Recovery, High Signal-to-Noise Ratio, and High Responsivity Fabricated via a Simple Defect-Generating Process," *Scientific reports* 6, no. 1 (2016): 31991, https://doi.org/10.1038/srep31991.

32. U. Pandey, N. Pal, A. Ghosh, S. Suman, S. Biring, and B. N. Pal, "Blue Sensitive Sub-Band Gap Negative Photoconductance in SnO_2/TiO_2 NP Bilayer Oxide Transistor," *Nanoscale* 16, no. 17 (2024): 8504–8513, https://doi.org/10.1039/D4NR00406J.

33. S. Hazra, S. V. Singh, S. Dahiya, P. K. Aich, and B. N. Pal, "Solution-Processed Ag-TiO_2 Nanostructure-Based Schottky Junction Thin Films for Narrowband Hot-Electron Photodetectors," *ACS Applied Nano Materials* 6, no. 16 (2023): 15119–15127, https://doi.org/10.1021/acsanm.3c02736.

34. U. Pandey, A. K. Yadav, N. Pal, P. K. Aich, and B. N. Pal, "Enhanced Sub-Band Gap Photosensitivity by an Asymmetric Source–drain Electrode Low Operating Voltage Oxide Transistor," *Journal of Materials Chemistry C* 11, no. 43 (2023): 15276–15287, https://doi.org/10.1039/D3TC02911E.

35. N. Pal, U. Pandey, S. Biring, and B. N. Pal, "Solution Processed Low-Voltage Metal-Oxide Transistor by Using TiO_2/Li–Al_2O_3 Stacked Gate Dielectric," *Journal of Materials Science: Materials in Electronics* 33, no. 12 (2022): 9580–9589.

36. R. Chakraborty, N. Pal, U. Pandey, et al., "Fabrication of Non-Volatile Memory Transistor by Charge Compensation of Interfacial Ionic Polarization of a Ferroelectric Gate Dielectric," *Applied Materials Today* 33 (2023): 101862, https://doi.org/10.1016/j.apmt.2023.101862.

37. N. K. Chourasia, A. Sharma, V. Acharya, N. Pal, S. Biring, and B. N. Pal, "Solution Processed Low Band Gap Ion-Conducting Gate Dielectric for Low Voltage Metal Oxide Transistor," *Journal of Alloys and Compounds* 777 (2019): 1124–1132, https://doi.org/10.1016/j.jallcom.2018.10.163.

Supporting Information

Additional supporting information can be found online in the Supporting Information section.

Supporting File: aelm70433-sup-0001-SuppMat.docx.